Polyhedron 224 (2022) 116028

Contents lists available at ScienceDirect

Polyhedron

journal homepage: www.elsevier.com/locate/poly

Manipulation of the cyanido-bridged Fe_2W_2 rhombus in the crystalline state: Co-crystallization, desolvation and thermal treatment

Jedrzej Kobylarczyk [a,b,*], Paweł Pakulski [a], Izabela Potępa [a], Robert Podgajny [a,*]

[a] Faculty of Chemistry, Jagiellonian University, ul. Gronostajowa 2, 30-387 Krakow, Poland
[b] Institute of Nuclear Physics PAN, Radzikowskiego 152, 31-342 Kraków, Poland

ARTICLE INFO

Keywords:
Secondary building blocks (SBBs)
Cyanido-bridges
Co-crystals
Charge transfer
Mixed-valence

ABSTRACT

We present the new cyanido-bridged rhombus $\{[Fe^{II}(TPMA)]_2[W^{V}(CN)_8]_2\}^{2-}$ (Fe_2W_2) (TPMA = tris(2-pyridylmethyl)amine) cluster as a potential Secondary Building Block (SBB) for construction of polynuclear molecular materials. Fe_2W_2 is formed easily in self-assembly process between $[Fe^{II}(TPMA)]Cl_2$ and $TBA_3[W(CN)_8]$ in H_2O/MeOH media, and was co-crystallized in $(TBA)_2\{Fe_2W_2\}\cdot 2H_2O$ (**1**), and $(TBA)_2\{Fe_2W_2\}\cdot m$MeOH$\cdot n H_2O$ (**2**) solvated salts, and in $(TBA)_2\{Fe_2W_2\}\cdot H_3PG\cdot m$MeOH$\cdot n H_2O$ (**3**) (H_3PG = phloroglucinol, 1,3,5-trihydroxybenzene; co-former) solvated co-crystal salt. Crystals of **1** undergo reversible SCSC transformation $\mathbf{1} \rightleftarrows \mathbf{1^{deh}}$ upon controlled dehydration and rehydration processes, whereas crystals of **2** reveal anisotropic thermal expansion during heating from 100 K to room temperature. Both processes involve changes of the selected intermolecular distances or local molecular reorientation involving intermolecular cation–anion and anion-anion contacts. $[Fe^{II}(TPMA)(\mu\text{-}NC)_2]$ moieties reveal low-spin (LS) state in each case, however, conformation of the Fe_2W_2 rings varies from the "staggered" in **1**, nearly "eclipsed" in **2** to fully "eclipsed" in **3**, which is attributed to various hydrogen bond $_{CN}N\cdots H\text{—}O$ schemes involving the terminal cyanido ligands in $[W(CN)_8]^{3-}$ and co-crystallizing molecules. In particular, the conformation of Fe_2W_2 in **3** is fully controlled by an unprecedented cyclic double hydrogen bond $\{Fe_2W_2\}\cdots H_3PG$ synthon, H_3PG forming a bridge over the Fe_2W_2 rhombus plane through binding the opposite $[W(CN)_8]$ corners. This arrangement is co-stabilized by close-to-parallel contacts of H_3PG with TPMA walls protruding out of the rhombus plane. The Fe_2W_2 rhombus is stable in MeOH solution and shows notable affinity to H_3PG in the gas phase, which was confirmed by ESI-MS data. UV–Vis-NIR spectroscopy discloses an optical $Fe^{II} \rightarrow W^{V}$ MMCT transition and mixed-valence $Fe^{II//III}$-$W^{V/IV}$ electronic ground state.

1. Introduction

Polycyanidometallates are attractive building blocks for the design and construction of polynuclear complexes showing spin-state-based properties for functionality, i.e. large span of spin value and magnetic anisotropy in the ground state for the single-molecule magnet (SMM) and single-chain magnet (SCM) behavior, or 2-dimensional (2D) and 3-dimensional (3D) long-range magnetic ordering (LRMO). Further on, the design of more advanced systems can be obtained *via* incorporation of other functionalities, for example: (*i*) structural transformations occurring due to solvent or molecular guest removal, uptake or exchange, (*ii*) switchable spin-structure behaviour based on electron transfer (ET) or spin-crossover (SCO), or/and (*iii*) incorporation of non-centrosymmetry and chirality of space group, luminescent behaviour or conductivity; such combinations allow to increase the dimensionality of the functional {-1,0,1} states platform for external manipulation [1–17].

Parallel to that, the concept of Secondary Building Blocks (SBBs) (originating from the field of metal–organic frameworks, MOFs) [18] was considered as a design and construction tool for the construction of molecular materials. Following the pioneering work of J. R. Long and co-workers on aggregation towards giant cyanido-bridged clusters (up to 27-nuclear) [19], the 15-nuclear $\{M_9[W'(CN)_8]_6(MeOH)_{24}\}$ (M = Mn^{II}, Co^{II}) high-spin clusters [20,21], 5-nuclear $\{[Co^{II/III}(tmphen)^2]_3[Fe^{II}(CN)_6]_2\}$ (tmphen = 3,4,7,8-tetramethyl-1,10-phenanthroline) mixed-valence electrochemically non-rigid clusters [22], and 3-nuclear photoactive $\{Pt(NH_3)_4[Mo(CN)_8]_2\}^{4-}$ rods [23] were *hypothesized and evidenced* to serve as SBB substrates to obtain extended networks. This possible thanks to a propitious set of structural properties

* Corresponding authors at: Institute of Nuclear Physics PAN, Radzikowskiego 152, 31-342 Kraków, Poland (J. Kobylarczyk); Faculty of Chemistry, Jagiellonian University, ul. Gronostajowa 2, 30-387 Krakow, Poland (J. Kobylarczyk and R. Podgajny).
E-mail addresses: jedrzej.kobylarczyk@ifj.edu.pl, jedrzej.kobylarczyk@doctoral.uj.edu.pl (J. Kobylarczyk), robert.podgajny@uj.edu.pl (R. Podgajny).

https://doi.org/10.1016/j.poly.2022.116028
Received 31 March 2022; Accepted 2 July 2022
Available online 6 July 2022

towards realization of this concept: (*i*) the exposed Lewis acid or/and Lewis base sites toward external coordination, and (*ii*) essential reproducibility and stability in solution.

In this work we re-direct our interest to one of the smallest possible aggregate realizing the square planar topology. Various combinations of metal-ligands sets were embedded in this backbone making it ubiquitous in magnetochemistry of polycyanidometallates [24–34]. Following the prosperity of some of the Co_2Fe_2 squares as switchable units active both in solution and in the solid state [25,26,28–32], the $[M(CN)_8]^{n-}$ (M = W, Mo) based rhombs Mo_2Fe_2 [33] or W_2Fe_2 [34] and other topological motifs [35–41] were shown to exhibit thermal and light-induced switchable character in the crystalline state. The Fe-$[M(CN)_8]$ pairs should be considered with a particular attention, due to various possible channels for spin-structure conversions evidenced recently, e.g. in the systems involving separately photo-induced spin state conversion $^{LS}Fe^{II} \rightarrow {}^{HS}Fe^{II}$ or $^{LS}M^{IV} \rightarrow {}^{HS}M^{IV}$ [39] as well as pronounced competition between Fe^{II}-centred SCO and $Fe^{II/III}$-$[W(CN)_8]^{3-/4-}$ ET processes [36,38].

Considering the above issues we introduce hereby the new rhombus, cyanido-bridged $[Fe^{II}(TPMA)]_2[W^{V}(CN)_8]_2\}^{2-}$ (Fe_2W_2) (TPMA – tris(2-pyridylmethyl)amine) SBB, the [Fe(TPMA)L_2] (L – ligand) moieties considered previously as a source of SCO transition [42–60]. In search of the new switchable molecular platforms we make our Fe_2W_2 a subject of manipulation through the solvation state in crystals [61], and through co-crystallization with the non-covalent interaction generator H_3PG (phloroglucinol, 1,3,5-trihydroxybenzene), the latter strategy representing a new emerging mean for shaping the solid state properties of cyanido-bridged coordination based solids [28–30].

2. Results

2.1. Structural studies

2.1.1. Comparative description of 1, 2, and 3

The crystal structures of **1**–**3** at 100 K are closely related as they are composed of cyanido-bridged $\{[LS\text{-}Fe^{II}(TPMA)]_2[W^{V}(CN)_8]_2\}^{2-}$ rhombus clusters (Fe_2W_2) (Fig. 1), TBA^+ cations, and co-crystallizing molecules: two single H_2O molecule per one Fe_2W_2 rhombus in **1**, more numerous aggregated MeOH and H_2O molecules in **2**, and numerous aggregated MeOH and H_2O molecules accompanied by one H_3PG co-former molecule per one Fe_2W_2 in co-crystal salt **3**. The crystal parameters, solution and refinement parameters are shown in Table S1, Table S2, and Table S3. The asymmetric units are presented in Fig. S1-S8, and the most important metric parameter and shape features of Fe_2W_2 are shown in Table S4, Table S5, Table S6, and Fig. S9. Uniformity of bulk samples and their identity with examined single crystal was confirmed by PXRD patterns (Fig. S10).

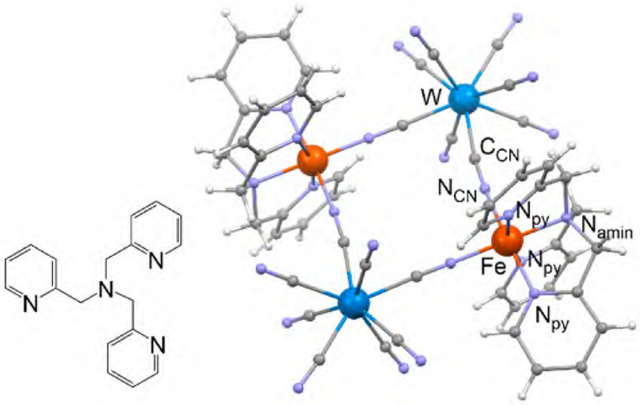

Fig. 1. The molecular structure of TPMA ligand and $\{[Fe(TPMA)]_2[W(CN)_8]_2\}^{2-}$, Fe_2W_2, rhombus cluster in **1**–**3**. Colours (spheres): cyan – W, brick – Fe, grey – C, pale blue – N, pale grey – H. Abbreviations: py – pyridine, amin – amine.

In the Fe_2W_2 clusters the average Fe-N bond lengths in the [Fe(TPMA)(μ-NC)$_2$] moieties are in the range 1.95–1.96 Å indicating the low spin (LS) state of Fe(II) ion in all compounds at 100 K. The angular distortion (bond angle) parameters $\sum$ (the sum of deviations of the 12 *cis N*-Fe-N angles from 90°) of 46.3° for **1**, 39.5° for **2**, 50.0° for Fe1 in **3**, and 42.6° for Fe2 in **3** differ notably from each other, however, are still at least twice smaller than those noted for the similar analogous high spin complexes. The shape measures of 0.342 (**1**), 0.261 (**2**), 0.365 (Fe1 in **3**) and 0.256 (Fe2 in **3**) (Table S5) go in line with the above dataset, still being in agreement with relatively small distortions from the ideal octahedron expected for LS complexes. The stability of the LS state of Fe (II) centres in the entire accessible temperature range 2 – 300 K was confirmed by the results of structural characterization (*see* Table S1-S3 and Fig. S10) and SQUID magnetometry (*see below* and *SI section*). The above features locates our compounds among the room temperature LS complexes with *cis*-Fe(N^{TPMA})$_4$($N\equiv$C-Me)$_2$ coordination environment [42,43,62,63]. On the contrary, HS configuration and SCO transition below RT for *cis*-Fe(N^{TPMA})$_4$($N\equiv$C-Me)$_2$ complexes might be achieved by attachment of bulky group at the *ortho*- position with respect to the coordinated N atom of pyridine [42]. SCO transitions was also widely observed for *cis*-Fe(N^{TPMA})$_4$(N^{L})$_2$ or *cis*-Fe(N^{TPMA})$_4$(*N*-N^{L}) species, where L = NCS or NCSe [44–46], diamines, amino-imines and diimines [47–51], dicyanamide, tricyanamide and their derivatives [51–54], or cyanometalate complexes [55–60].

The shape measures for $[W(CN)_8]$ moieties indicate domination of SAPR-8 in **1** ($S_{SAPR\text{-}8}$ = 0.576, $S_{TDD\text{-}8}$ = 0.994, $S_{BTBR\text{-}8}$ = 1.683), significant contribution of BTPR-8 in **2** ($S_{SAPR\text{-}8}$ = 0.921, $S_{TDD\text{-}8}$ = 1.196, $S_{SAPR\text{-}8}$ = 1.251), whereas in **3** we observe two different $S_{SAPR\text{-}8}$ measures, 0.316 for W1 ($S_{TDD\text{-}8}$ = 1.742, $S_{SAPR\text{-}8}$ = 1.886), and of 0.652 for W2 ($S_{TDD\text{-}8}$ = 1.347, $S_{SAPR\text{-}8}$ = 1.249), the former one indicating the geometry very close to the ideal square antiprism (Table S6, Fig. S9). The cyanido-bridges only slightly deviate from linearity, each compound revealing one Fe—N—C angle closer to 180° and another one between 170 and 175°. In all **1**–**3** structures Fe_2W_2 rhombs show notable distortion from the perfect square shape illustrated by the Fe···W···Fe angles in the range of 82.0–83.4°, and W···Fe···W angles in the range of 98.0–96.1°. However, while in **1** Fe_2W_2 rhombs are perfectly flat, in **2** and **3** they are slightly distorted from planarity, as shown by the dihedral angles close to 170° and 173°.

One of the focal features within our series is the incorporation of a triple point H_3PG hydrogen bond donor in co-crystal salt **3**. This molecular tecton has been widely considered in studies on co-crystals [64–74] or liquid crystalline phases [75–77] in the context of topological reactivity [64], combinatorial or modular synthetic strategies [65,75], proton disorder [66], drugs fabrication improvement [67], luminescence switching [68], switchable magnetic properties [29], chiral properties and photonic materials [76] or overall molecular organization [29,69–74,77]. In **3**, H_3PG molecule possesses the C_s [66] geometry, and is in direct contact with two Fe_2W_2 rhombs, three TBA^+ cations and some solvent molecules (Fig. 2a, b). The most peculiar feature of this arrangement is the new original cyclic hydrogen bond synthon between H_3PG and Fe_2W_2 rhombus exploiting $_{CN}N\cdots H\text{-}O_{H3PG}$ arrays, H_3PG forming a bridge over the Fe_2W_2 rhombus plane through binding the opposite $[W(CN)_8]$ corners (Fig. 2c). This arrangement is co-stabilized by close-to-parallel contacts of H_3PG with TPMA walls protruding out of the rhombus plane.

The metric parameters, N···O distances of 2.75 Å and 2.83 Å, N···H distances of 1.96 Å and 1.97 Å, and O—H···N angles of 151.1° and 178.1°, respectively, indicate a considerable strength of interactions within each contact. The computational evaluation of energy gain is beyond the scope of this work, however we estimate that the stability of such aggregate might be notable due to the additional anchoring effect. Interestingly, the concentration Fe: W: TBA^+: H_3PG ratio in MeOH solution close 1: 1: 3: 1 or 1: 1: 3: 2 resulted in the same isomorphous architecture, yet modeled with the fractional (close to $^1/_4$) occupancy of

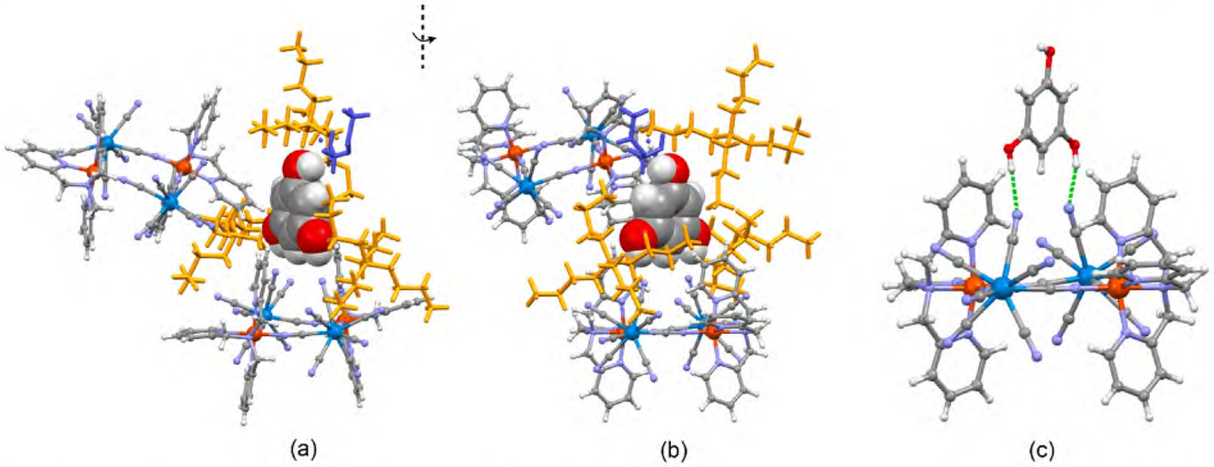

Fig. 2. (a,b) Two projections of molecular surroundings of H_3PG molecule in **3**. (c) The original cyclic hydrogen bond synthon between H_3PG and Fe_2W_2 rhombus exploiting the $_{CN}N\cdots H\text{-}O_{H3PG}$ arrays (green dotted lines). Colours: H_3PG (spacefill or spheres), grey – C, red – O, pale grey – H; Fe_2W_2 (spheres) cyan – W, brick – Fe, grey – C, pale blue – N, red – O, pale grey – H; yellow sticks – TBA^+ cations; navy blue sticks – crystallization solvent molecules.

each non-hydrogen H_3PG atom only, whereas its full occupancy was achieved only with the relevant 1: 1: 3: 8 ratio, assuring the minimum 4-fold excess of co-former over Fe_2W_2 rhombs. However, formation of this synthon definitely competes with other weaker but more abundant interactions, including also interactions involving solvent molecules governed by the polarity of MeOH/H_2O media. The ESI-MS data for MeOH solutions of Fe_2W_2 hydrated salt **1** and Fe_2W_2 co-crystal salt **3** shed some light on the mutual affinity between Fe_2W_2 and H_3PG. The spectra obtained in the negative ionization mode do not differ significantly from each other, exhibiting the presence of two significant isotopic patterns easily assignable to the pure complete cyanido-bridged $\{Fe_2W_2\}^{2-}$ cluster ($m/z = 783.07$), or to the relevant $\{Fe_2W_2,TBA\}^-$ aggregate ($m/z = 1718.42$), and a large variety of patterns attributable to oligomeric Fe_xW_y-based singly, doubly or triply charged aggregates (Fig. 3). Interestingly, the spectra obtained in positive ionization mode differ significantly. The spectrum of **1** is dominated by the isotopic.

patterns assignable to singly charged Fe complex based fragments of m/z between 500 and 1000 D, and shows only three rather less intense isotopic patterns related to some low nuclear Fe_xW_y based aggregates of rather unclear exact composition (Fig. S11). On the contrary, the spectrum of **3** does not contain the sole Fe complex patterns and is dominated by the several notable isotopic patterns attributable to Fe_2W_2 based aggregates (Fig. 4 and Fig. S12). The pattern of $m/z = 2202.98$ is easily assignable to the salt like $\{Fe_2W_2, TBA_3\}^+$ aggregate, whereas the pattern of $m/z = 1845.30$ is reasonably attributable to the co-crystal like solvated $\{Fe_2W_2,(H_3PG)_2(MeOH)_3(H_2O)–3H\}^+$ aggregate. The exact composition of other patterns, dominating this spectrum, is rather unclear, however, they definitely contain singly charged Fe_2W_2 or FeW based aggregates, probably being the product of more complicated fragmentation.

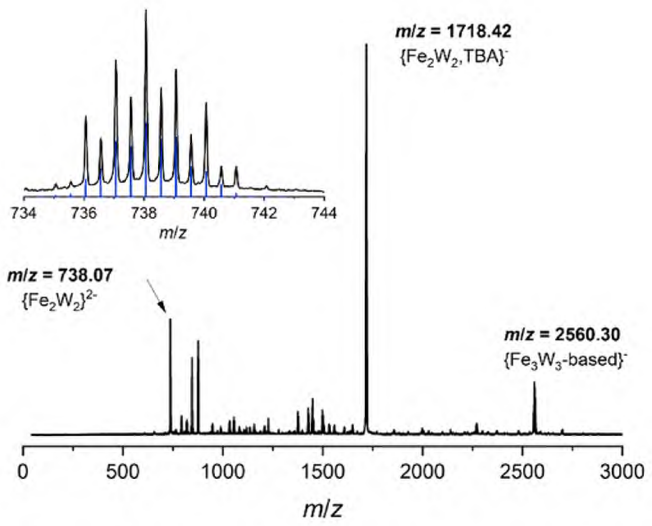

Fig. 3. The ESI-MS spectrum of the MeOH solution of **1** in negative ionization mode. The inset shows the isotopic pattern for a complete cyanido-bridged $\{Fe_2W_2\}^{2-}$ cluster ($m/z = 783.07$) together with the simulation. The whole spectrum is almost identical with the relevant ESI-MS spectrum of the MeOH solution of **3** in negative ionization mode. Both spectra also exhibit the presence of various oligomeric Fe_xW_y-based singly, doubly or triply charged aggregates.

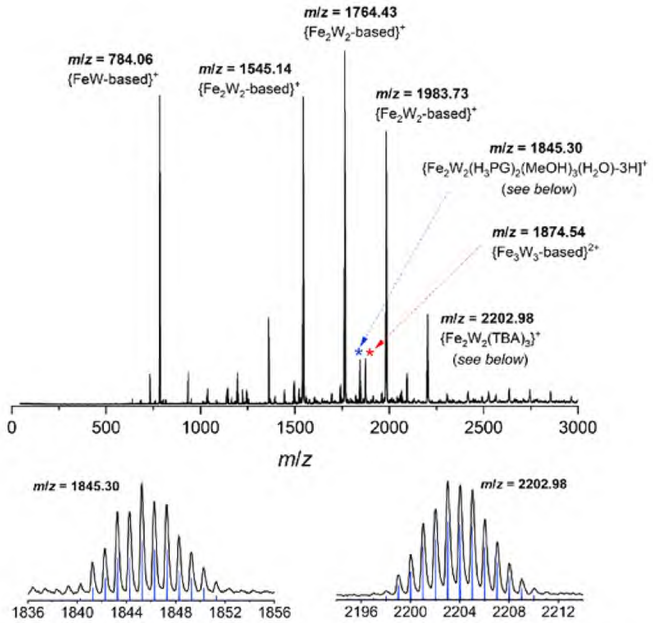

Fig. 4. The ESI-MS spectrum of MeOH solution of **3** in positive ionization mode. The bottom panel shows isotopic patterns assignable to $\{Fe_2W_2(H_3PG)_2(MeOH)_3(H_2O)–3H\}^+$ aggregate ($m/z = 1845.30$) or to $\{Fe_2W_2(TBA)_3\}^+$ ($m/z = 2202.98$) aggregate together with the simulations. The spectrum is notably different from that of the ESI-MS spectrum of **1** in the positive ionization mode and reveals also the presence of various motifs based on polymetallic singly or doubly charged Fe_2W_y aggregates.

The signature of the $\{Fe_2W_2,(H_3PG)_2(MeOH)_3(H_2O)–3H\}^+$ aggregate and overall difference spectra of **1** and **3** in positive ionization mode support non-negligible mutual affinity of Fe_2W_2 and H_3PG suggested by the structural data for **3**. A convergent character of the described $\{[Fe_2W_2];[H_3PG]\}$ synthon differs significantly from the divergent binding of SCO Co_2Fe_2 squares by the H_3PG towards the honeycomb network reported previously [29], which might be the result of differences in the molecular structure of both clusters and different reaction conditions used in the syntheses.

The differences in crystallization media and the additional presence of H_3PG do not influence the coordination topology of the Fe_2W_2 rhombs, however, reveal a notable impact on the structural conformation (Fig. 5). The top panel in Fig. 5 presents the projections along the W···W direction, whereas the bottom panel shows the projections after rotation of some acute angle along the indicated axis. The solvent molecules staying in contact with the cluster fragments, and the relevant separations $_{CN}$N···H (Fig. 5, top panel) and $_{CN}$N···O (bottom panel) are also indicated. In compound **1**, the front $[W(CN)_8]$ moiety reveals a staggered-like conformation of terminal cyanido ligands in respect to the rear one, whereas in **3** one observes an eclipsed like conformation (top panel). Examination of another projection (Fig. 5, bottom panel) indicates a close to parallel orientation of the square like faces of both $[W(CN)_8]$ in **1**, while in **3** the vectors normal to such faces of two different $[W(CN)_8]$ are very far from parallel orientation. Compound **2** shows one of the intermediate conformations, rather closer to that of **3** than to that of **1**. Moreover, some differences in mutual orientations between the relevant TPMA fragments are also observed. The above features are attributable, in general, to molecular surroundings, and are most probably governed by the position, strength and degree of rigidity of hydrogen bond donors set in respect to the terminal cyanido ligands as the first choice hydrogen bond acceptor in the system. In **1**, H_2O molecules are connected to $[W(CN)_8]$ at the side peripheral region of the cluster, whereas in **2** and **3** hydrogen bond donors are located above the cluster interior. Moreover, in **3**, H_3PG provides a much more rigid and stronger double H-donor, the latter being the consequence of known larger acidity of phenols compared to H_2O or MeOH.

Crystal packing of **1** is dominated by intercluster $Fe_2W_2···Fe_2W_2$ contacts along *a*, *b*, and *c* directions (Fig. S13), whereas in **2** and **3** one observes only 1-dimensional arrangement of Fe_2W_2 clusters along the [101] direction (Fig. S14) and along the *a* direction (Fig. S15), respectively; in **3** such arrays are connected by additional local contacts resulting in a ladder-like supramolecular topology.

Three types of intercluster contacts might be distinguished along this series (Fig. 6). The topologically identical parallel side-to-side contacts $[W(CN)_8]···[Fe(NC)_2(TPMA)]$ involving multiple $_{CN}$N···H-$C_{TPMA,ring}$ and $_{CN}$N···H-$C_{TPMA,chain}$ synthons are consequently observed both in **1**, **2** and **3** (Fig. 6a), whereas the additional interdigitation type contacts were noted only in **1** and **3** (Fig. 6b,c). In **1**, the "parallel" interdigitation occurs along the *c* direction, with the TPMA pyridine rings pointing towards the pockets formed by terminal cyanido ligands of $[W(CN)_8]^{3-}$ moiety (Fig. 6b). These contacts are accompanied by 1-dimensional hydrogen bond like $\{Fe_2W_2(···H—O—H)_2\}_\infty$ chains exhibiting the cyclic synthons based on bent $_{CN}$N···H—O—H···N_{CN} arrays with the N···O separations of 2.96 and 3.02 Å, and N···H separations of 2.13 and 2.18 Å indicating rather weak character of these interactions. In addition to that, the "perpendicular" interdigitation occurs in **1** and **3** of 1-dimensional and local character, respectively (Fig. 6c). The side-to-side synthon in **1**, **2**, and **3** might definitely be considered as the result of molecular matching and self-recognition between Fe_2W_2 clusters.

The TBA^+ cations are distributed around the Fe_2W_2 rhombs in quite a regular manner in all structures (Fig. 7). The $TBA^+···Fe_2W_2$ contacts are realized through the multiple $_{cation,chain}$C-H···N_{CN} and $_{cation,chain}$C-H···$centroid_{TPMA,ring}$ synthons, and involves a kind of TBA^+ chains ends trapping within the "shells" formed by the TPMA ring walls or by the terminal CN^- ligands protruding out of the **Fe_2W_2** rhombus. This occurs either at the periphery of Fe_2W_2 rhombs in the pockets formed by the perpendicular rings of the one TPMA ligands, or close to the interior of the ring in the pocket formed by close-to-parallel rings of TPMA ligands coordinated to different Fe centres. The former arrangement is characteristic for all described compounds **1**, **2** and **3**, whereas the latter one

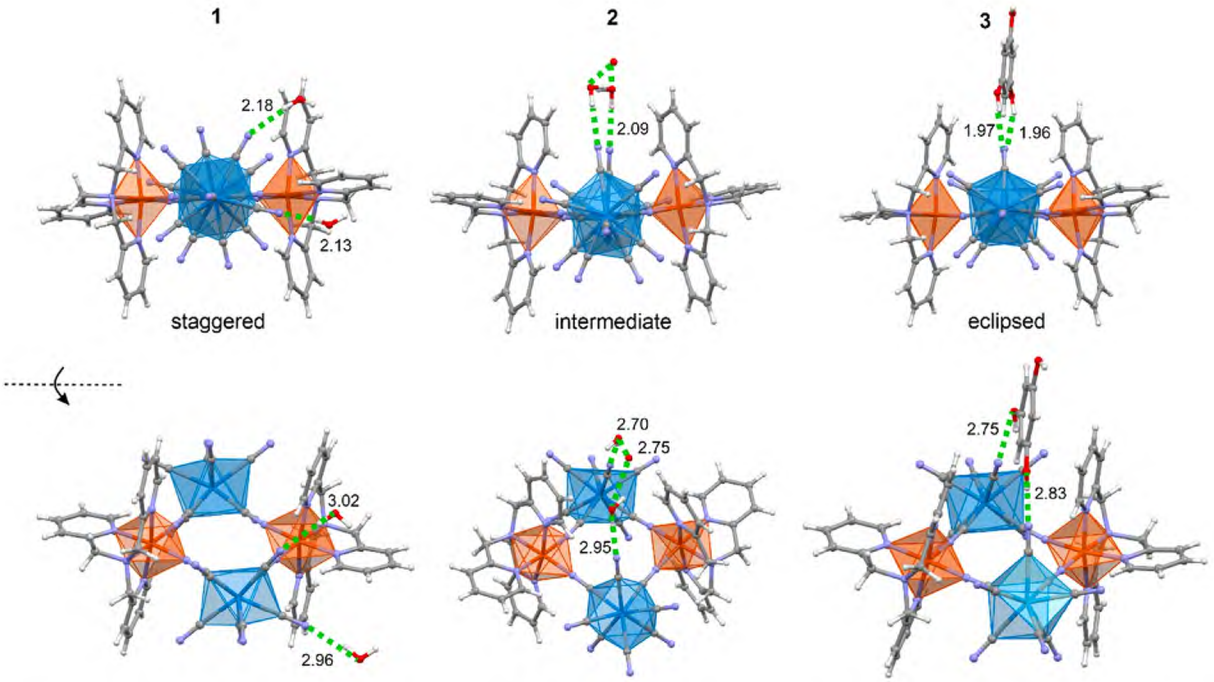

Fig. 5. Structural conformation of Fe_2W_2 rhombs in **1**, **2**, and **3**. The conformations differ in a mutual orientation of $[W(CN)_8$ moieties within the rhombus, which is represented by the staggered-like and eclipsed-like projections shown in the top panel. The N···H-$O_{solvent}$ or N···H-O_{H3PG} contacts together with the N···H distances (top panel) and the relevant N···O distances (bottom panel) are also shown. Colours: cyan polyhedral – W, brick polyhedral – Fe, grey spheres – C, pale blue spheres – N, red spheres – O, pale grey spheres – H, green dotted lines – hydrogen bonds.

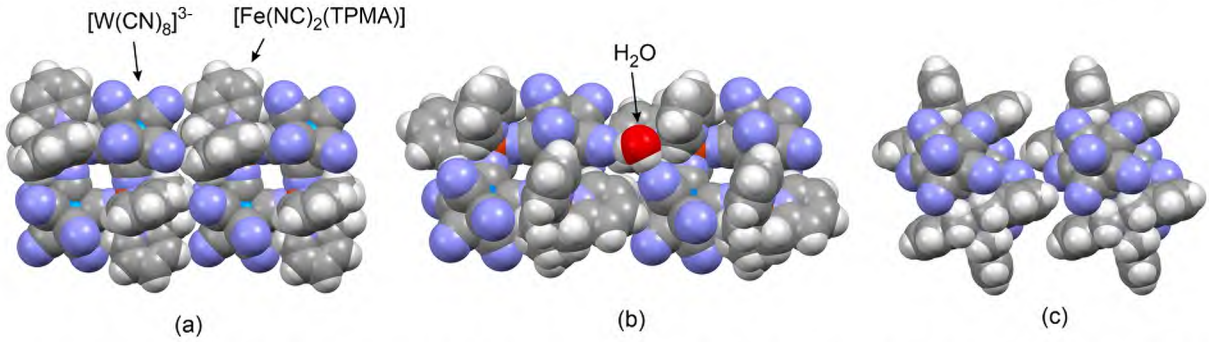

Fig. 6. Intermolecular contacts between the neighbouring Fe_2W_2 rhombs involving [Fe(NC)$_2$(TPMA)] and [W(CN)$_8$] moieties: (a) multiple side-to-side $_{CN}$N···H-C$_{TPMA,ring}$ and $_{CN}$N···H-C$_{TPMA,chain}$ synthons in all **1**, **2** and **3** structures, (b) "parallel" interdigitation synthons assisted by $_{CN}$N···H—O—H···N$_{CN}$ hydrogen bonds array in **1**, and (c) "perpendicular" interdigitation synthons in **1** and **3**. Colours (spacefill): cyan – W, brick – Fe, grey – C, pale blue – N, red – O, pale grey – H.

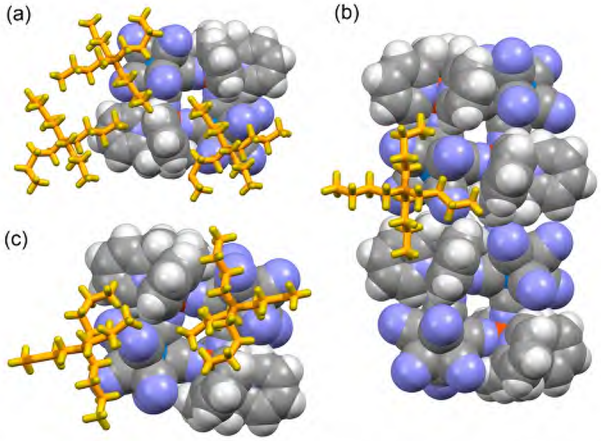

Fig. 7. Intermolecular contacts between the Fe_2W_2 rhombs (spacefill) and TBA$^+$ cations (yellow sticks) in **1** (a), **2** (b), and **3** (c). These contacts involves the multiple $_{cation,chain}$C-H···N$_{CN}$ and $_{cation,chain}$C-H···centroid$_{TPMA,ring}$ synthons together with the mechanical like trapping of the TBA$^+$ chain end within the cavity formed by the TPMA ring walls and the terminal CN$^-$ ligands protruding out of to the Fe_2W_2 plane. Colours: Fe_2W_2 (spacefill): cyan – W, brick – Fe, grey – C, pale blue – N, pale grey – H; TBA$^+$ cations – yellow sticks.

was noted only in **1** and **3**. Notable cations aggregation exploiting the contacts between C—H groups can be also observed.

Contrary to hydrate compound **1**, compounds **2** and **3** contain many co-crystallization components, MeOH with some addition of H_2O in both cases, and co-former H_3PG in **3**. Solvent molecules tend to aggregate in the separate channels along the direction [101] in **2**, and along the direction *a* in **3**, showing considerable degree of structural disorder. They are expected to co-stabilize the structures through the C—H···O$_{solvent}$, C—H···N$_{CN}$ and $_{solvent}$O-H···N$_{CN}$ interactions.

2.1.2. *Reversible SCSC dehydration* ***1*** ⇄ ***1^{deh}***

Compound **1** loses coordination H_2O under heating within temperature range 60 – 90 °C under the N_2 flow to produce the dehydrated phase **1^{deh}**. The SCSC transformation occurs without a loss of a single-crystal character, which allowed full structural characterization of this process. The removal of H_2O molecules leads to rather moderate structural changes. The crystallographic parameters obtained at 100 K change slightly from $a = 11.7464(4)$ Å, $b = 12.9824(5)$ Å, $c = 14.4131(5)$ Å, $\alpha = 87.989(1)°$, $\beta = 78.462(1)°$, and $\gamma = 87.840(1)°$ to $a = 11.5530(5)$ Å $b = 12.9945(5)$ Å, $c = 14.5143(6)$ Å, $\alpha = 86.067(1)°$ $\beta = 78.714(1)°$ $\gamma = 88.624(1)°$ (Table S1). A shortening of *a* period (*ca.* 1.7 %) and minor elongation of the *c* period (*ca.* 0.7 %), together with some changes of angles led to a rather small decrease in cell volume *V* from 2151.15(13) Å^3 to 2131.67(15) Å^3 (*ca.* 0.92 %). Interestingly, along the direction *c* (the direction of hydrogen-bonded chain in **1**) the intercluster separation increase slightly, which is illustrated by the increase of the relevant Fe···W distances from 9.38 Å to 9.49 Å (Fig. 8) owing to the loss of the H_2O supramolecular connectors. The most recognizable molecular movement due to the SCSC transformation is *ca.* 1 Å shift of the TBA$^+$ butyl arm #1 towards the empty space available after water removal, which is also accompanied be a less pronounced shift of arm #2 towards the interior of the relevant Fe_2W_2 rhombus, and a shift of arm #3 towards the nearest cluster's periphery, both illustrated by the *ca.* 0.3 Å decrease of the relevant distances. The other structural parameters do not change significantly. The exposition of crystals of **1^{deh}** to air led to the restoration of the starting composition and structural arrangements, which is shown by identical structural parameters of **1^{reh}** and **1**. The heating of **1** and **1^{deh}** to room temperature did not lead to the occurrence of plausible SCO transition (see structural parameters in ESI section).

2.1.3. *Anisotropic thermal expansion of* ***2***

The controlled heating of **2** lead to a slightly anisotropic thermal expansion, which was illustrated by the change of crystal lattice parameters from $a = 27.6833(17)$ Å, $b = 19.0695(12)$ Å, $c = 24.293(2)$ Å, $\beta = 120.4810(10)°$ to $a = 27.8311(15)$ Å, $b = 19.5153(11)$ Å, $c = 24.6038(13)$ Å, $\beta = 120.6960(10)°$ (Table S2 and Table S3). The increase of parameter *a* of 0.5 %, parameter *b* of 2.2 %, and of parameter *c* of 1.3% together with a minor change in β angle correlates with the *ca.* 4 % increase of the volume cell, from 11052.2(14) Å^3 to 11490.8(11) Å^3. Such expansion might be correlated with direct intercluster contacts along the [101] direction only, and due to a significant number of solvent molecules providing a notable degree of freedom to direct the expansion in an anisotropic manner. This is unlike the case of **1** and **1^{deh}**, where the expansion is rather isotropic and not exceeding 1 % of elongation in the case of each period, with the volume change of 3.2 % and 2.8 %, respectively (Table S1 and Table S3). In these architectures we observed the domination of more rigid intercluster contacts along all three orthogonal directions, which control intermolecular interactions in a more isotropic manner.

2.2. *Physicochemical characterization*

The representative UV–VIS-NIR diffuse reflectance spectrum for **1** in the range of 200–1500 nm together with the absorption spectrum of the relevant MeOH solution is presented in Fig. 9. The location of the distinguishable absorption bands **A**-**E** in both characteristics are rather convergent with each other, which confirms the stability of Fe_2W_2 chromophore in solution, in agreement with ESI-MS data. The composed absorption marked as **A**-**D** in the range 200–600 nm is assignable to the individual [Fe^{II}(TPMA)(μ-NC)$_2$] and [W^V(μ-CN)$_2$(CN)$_6$] moieties. In this range [W(CN)$_8$]$^{3-}$ anion is expected to exhibit LMCT transitions of the maxima around 250 nm and in range of 350–400 nm, as represented by

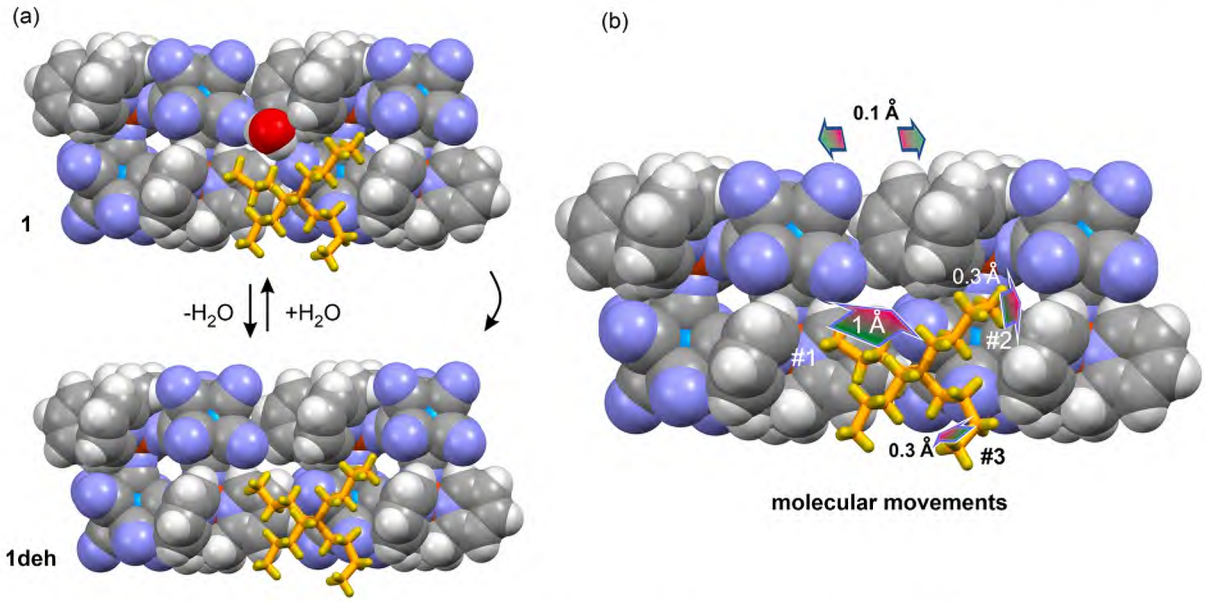

Fig. 8. Reversible dehydration **1**⇄ **1deh** (a) and accompanying directions of molecular movements (b). Colours: Fe_2W_2 (spacefill): cyan – W, brick – Fe, grey – C, pale blue – N, red O, pale grey – H; TBA^+ cations – yellow sticks.

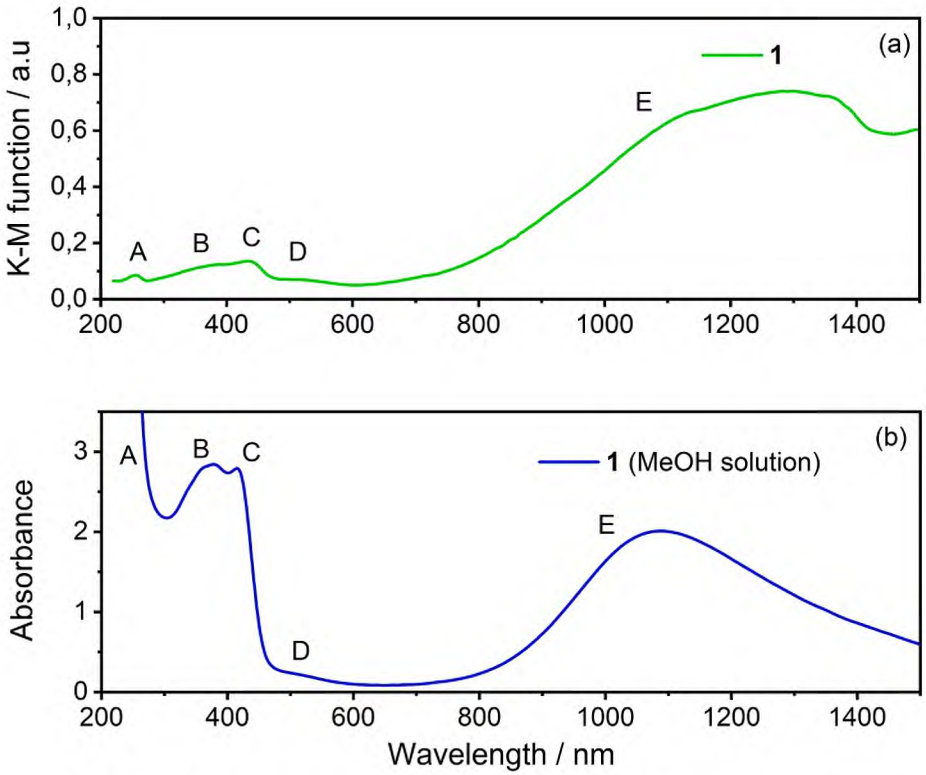

Fig. 9. The UV–VIS-NIR spectra for **1** in the solid state (Kubelka-Munk function) (top panel) and in MeOH solution (Absorbance, $c_{Fe2W2} = 0.26$ mmol dm^{-3}) (bottom panel). Labels **A-D** indicate spectral features of the individual $[Fe^{II}(TPMA)(\mu\text{-}NC)_2]$ and $[W^{V}(\mu\text{-}CN)_2(CN)_6]$ moieties, whereas label **E** mark the band assigned to the MMCT transition $^{LS}Fe^{II} \rightarrow W^{V}$.

A and **B** [78,79]. The electronic absorption in the UV range must also include the IL absorption of TPMA and MLCT of the iron(II) moiety. The bands marked as **C** and **D** in the range 400–600 nm can be assigned to the LF absorption of $[^{LS}Fe^{II}(TPMA)(\mu\text{-}NC)_2]$ moiety [34,80,81]. A notably intense broad and complex absorption band with the maximum at *ca.* 1280 nm in the solid state and at 1085 nm in MeOH solution, marked with **E,** dominates the NIR range and should be definitely attributed to the MMCT transition $^{LS}Fe^{II} \rightarrow W^{V}$ through cyanido-bridges [34,82], as a signature of mixed-valence $Fe^{II/III}$-$W^{V/IV}$ electronic ground state. The colouration of compounds **2** and **3** as well as of the phases obtained through the dehydration or thermal treatment are very similar to **1**, thus, the spectra of **1** might be treated as representative for the whole series.

IR spectra of **1**, $\mathbf{1}^{deh}$, **2**, and **3** are presented in Fig. S16 and Fig. S17. The high energy region of the mid IR range shows broad bands assigned to the ν(O—H) vibrations of co-crystallization solvent and H_3PG

molecules, co-existing with the separate peaks of ν(C—H) vibrations of TPMA ligand (C–H_{ring} and C–H_{chain} fragments), TBA^+ cations (C–H_{chain} fragments) and H_3PG (C–H_{ring} fragment). In the case of **1** and **2** ν(O—H) vibrations are represented in the 3650–3200 cm^{-1} range with the distinct transmittance minima close to 3500 cm^{-1}, whereas for **3** the additional transmittance minimum is observed at 3224 cm^{-1} and attributed to the vibration of O—H bonds of H_3PG. The region of the stretching vibration of cyanido-ligands ν(C≡N) exhibits strong peaks in the range 2170–2120 cm^{-1} for **1** and for **2**, and in the range 2170–2110 cm^{-1} for **3**. The patterns differ from each other: **1** reveals sharp spectral contour with distinct features at 2153 s, 2148 m, 2137 m(sh), 2134 s, and 2130 m(sh) cm^{-1}, whereas **2** and **3** show rather oval spectral shapes with 2153 s and 2138(sh) cm^{-1} components, and 2153 s, 2141 s, and 2130(sh) components, respectively. Such patterns are rather supportive for pentavalent tungsten in $[W(CN)_8]^{3-}$ [83] in line with structural and UV–Vis data. The difference in shapes in this region might be due to the difference in the complete sets of hydrogen bond donors, including O—H groups of solvent molecules and H_3PG, and an overwhelming number of C—H groups provided by TBA^+ cations and aromatic rings. Finally, the fingerprint region exhibits the complex pattern composed of the peaks characteristic to the skeletal vibrations of the organic components of **1–3**. The dehydration **1** → $\mathbf{1}^{deh}$ leads to the total loss of the spectral features of H_2O molecules above 3200 cm^{-1}, and in the range 1690–1600 cm^{-1}, representing the ν(O—H) and $\delta(H_2O)$ (scissors) vibrations, respectively.

$\chi T(T)$ and $M(H)$ curves indicate the presence of the two separated unpaired electrons assignable solely to the presence of $[W(CN)_8]^{3-}$ complexes, in line with the previous results (Fig. S18 and S19).

3. Discussion

The occurrence of stable LS configuration along the whole series tends to be in line with the results obtained with the *cis*-$(\mathbf{N}^{TPMA})_4(\mathbf{N}{\equiv}C\text{-}Me)_2$ coordination sphere [42,43,62,63], considering similarity of the ligand field strength provided by MeCN and by cyanidometallates, and coordination constrains imposed by TPMA ligand. On the other hand, wide representation of SCO systems with other *cis*-coordinated counterparts accompanying TPMA [44–60], involving also those realizing square 3d-3d' topology [55–60] might have supported expectations to observe SCO transition. In general, cooperativity in the above systems is far from optimum, whereas SCO transitions in some of the known Fe-$[M^V(CN)_8]$ (M = Mo, W) systems might suffer the incomplete character [41,80,84] or need serious external stimulation (pressure effects, guest inclusion) to thrive [40]. SCO in $Fe_2[M(CN)_8]_2$ rhombs was realized by the use of 5-membered pyrazole or imidazole based ligands, according to one of the successful strategies towards tuning of the ligand field strength and overall geometrical constrains [33,34]. In the $Fe_2[W(CN)_8]_2$ rhombs involving exact *cis*-$(\mathbf{N}^{TPMA})_4(\mathbf{N}{\equiv}C\text{-}Me)_2$ coordination spheres (e.g. analogous to **1–3**) one also might expect the additional bulky groups (methyl, aryl etc.) coordinated in the *ortho* position to induce the transition, which will be checked in the future studies. Predictability of the Fe centre spin state in such systems, in general, is not a simple issue, as still limited systems are known, and due to the fact of possible competition with $Fe^{II/III}$-$[W(CN)_8]^{3-/4-}$ ET processes [36,38]. Unfortunately, the approach relying on the modification of the hydrogen bonds in the second coordination sphere, either through the controlled dehydration or by the introduction of novel original double hydrogen-bonded synthon, did fail, however, it might be involved in further studies in combination with the strategy of ligand modification. Nevertheless, the presented negatively charged Fe_2W_2 rhombs might be also considered as the SBBs controllable in solution for further studies on construction of branched trimetallic coordination and co-crystal type architectures.

4. Conclusions

We have demonstrated manipulations on cyanido-bridged $\{[Fe^{II}(TPMA)]_2[W^V(CN)_8]_2\}^{2-}$ Fe_2W_2 rhombus building blocks of the mixed-valence $Fe^{II/III}$-$W^{V/IV}$ electronic ground state through the co-crystallization with various sets of hydrogen bond donors involving co-crystallizing H_2O (**1–3**), MeOH (**2,3**), and H_3PG (**3**) molecules. Controlled dehydration **1** ⇄ $\mathbf{1}^{deh}$ and thermal treatment of **2** resulted in changes in the selected intermolecular distances or intermolecular reorientations. The conformation of the Fe_2W_2 rings might be shaped by different hydrogen bond $_{CN}N\cdots H{-}O$ schemes involving the terminal cyanido ligands in $[W(CN)_8]^{3-}$ and co-crystallizing molecules. Interestingly, conformation of Fe_2W_2 in solvated co-crystal salt **3** (different than those in **1** and **2**) is controlled by the unprecedented and elegant cyclic double hydrogen bond $\{Fe_2W_2\}\cdots H_3PG$ synthon, H_3PG forming a bridge over the Fe_2W_2 plane through binding the opposite $[W(CN)_8]$ corners. The stability of the Fe_2W_2 rhombus in the MeOH solution was confirmed, and its notable affinity to H_3PG in the gas phase was indicated. These observations make the anionic Fe_2W_2 rhombus an attractive secondary building block (SBB) for the construction of advanced multicomponent hybrid organic–inorganic architectures. While the LS state of Fe(II) is preserved in all presented crystalline phases, one might expect that the targeted modification of ligands might easily result in overcoming the barrier for the LS ⇄ spin HS transition. Considering possible self-assembly versatility and structural non-rigidity demonstrated in this study for the $\{[Fe^{II}(TPMA)]_2[W^V(CN)_8]_2\}^{2-}$ based solids, one might expect the emergence of the new family of switchable building blocks; our group focuses the current studies on this goal.

5. Experimental

5.1. Materials

$FeCl_2{\cdot}4H_2O$, L(+)-ascorbic acid, 2-(chloromethyl)pyridine, 2-(aminomethyl)-pyridine, solvents (MeOH, DCM, Et_2O etc.) as well as other basic chemicals used in synthesis were purchased from commercial sources (Sigma Aldrich, Idalia, Chemat) and used without further purification. The polycyanidometallate precursor, $K_4[W^{IV}(CN)_8]$ was synthesized by reduction of Na_2WO_4 in the presence of KCN and $NaBH_4$, followed by a subsequent oxidation of the reacting mixture with 30 % H_2O_2 and precipitation with ethanol [85]. The $TBA_3[W^V(CN)_8]$ was prepared by oxidation of $K_4[W^{IV}(CN)_8]{\cdot}2H_2O$ with $KMnO_4$ in 2 M HNO_3 water solution followed by precipitation with TBABr.

5.2. Syntheses

5.2.1. Synthesis of TPMA ligand

The current synthesis is an adaptation of the literature procedure [86]. 2-(chloromethyl)pyridine hydrochloride (39 g, 238 mmol) was dissolved in 100 mL of water in a 500 mL round-bottomed flask and this solution was chilled overnight in the fridge (4 °C) together with 100 mL of 5.3 M NaOH solution. Flask with chilled hydrochloride solution was placed in the ice bath (0 °C) and cold 5.3 M NaOH solution (45 mL total) was added in 5 mL portions. The last addition caused the reaction mixture to turn slightly red. Addition of 1 mL of 5.3 M NaOH resulted in a permanent red coloration. To this mixture a solution of 2-(aminomethyl)-pyridine in 200 mL DCM was added in one portion and flask was removed from the ice bath to warm up to room temperature. Next, 5.3 M NaOH was added dropwise on vigorous stirring at a very low rate (2 mL/h.) to keep the reaction mixture pH below 9.5. Reaction was stirred very intensely for 48 h. The mixture was then diluted with 100 mL of 15 % aqueous NaOH solution and organic phase was separated, dried over anhydrous $MgSO_4$ and evaporated to a brown oil. This was

extracted 4x100 ml of boiling diethyl ether. An oily residue that was not extracted into Et_2O was discarded. The collected extracts were evaporated to an oil, dissolved in ethyl acetate and precipitated with 60/90 petroleum ether. This off-white solid was collected on a G3 glass funnel, washed with petroleum ether and dried to give pure product. Yield: 9.27 g (27 %). ^{1}HNMR (MeCN-d3): 8.47 (m, 3H), 7.70 (m,3H), 7.59 (m,3H), 7.20 (m,3H), 3.81 (s,6H) (Fig. S20).

5.2.2. Synthesis of **1** and transformation to $\mathbf{1}^{des}$ and $\mathbf{1}^{reh}$

1 mL of a freshly prepared H_2O/MeOH solution (0.5 mL H_2O, 0.5 mL MeOH) of TPMA ligand (38.75 mg, 0.13 mmol) in was added dropwise to 3 mL of H_2O/MeOH solution (1.5 mL H_2O, 1.5 mL MeOH) of $FeCl_2{\cdot}4H_2O$ (19 mg, 0.096 mmol) and L(+)-ascorbic acid (1.0 mg, 0.006 mmol). The resulting solution was stirred for 5 min, then a solution of $TBA_3[W^V(CN)_8]$ (111.9 mg, 0.1 mmol) in 1 mL MeOH was added dropwise while stirring continuously. The reacting mixture was stirred for next 20 min, and then the vial was tightly closed and left for crystallization in room temperature. After 3–5 days yellow–brown crystals appeared. The crystals of **1** were identified as $(TBA)_2\{[Fe^{II}(TPMA)]_2[W^V(CN)_8]_2\}{\cdot}2H_2O$, based on SC-XRD measurements. The obtained crystals are stable in air and maintain crystallinity. The results of the CHN elemental analysis match to the values calculated from SC-XRD formula. Calculated for $(TBA)_2\{[Fe^{II}(TPMA)]_2[W^V(CN)_8]_2\}{\cdot}2H_2O$: C 50.5 %, H 5.7 %, N 18.2 %. Found: C 50.4 %, H 5.6 %, N 18.2 %. Phase purity and stability in air was confirmed by powder XRD data performed on dry crystallites as well as on crystallites under mother solution (Fig. S10).

The crystals of **1** can be thermally dehydrated. Dehydration process occur in 333 – 363 K during N_2 purge, producing dehydrated crystalline phase $\mathbf{1}^{deh}$ with formula $(TBA)_2\{[Fe^{II}(TPMA)]_2[W^V(CN)_8]_2\}$, identified by SC-XRD measurements. In order to avoid stress and crack of crystals during SC-XRD measurement, the best results were obtained by placing crystal of **1** in Apiezon N grease in stream of N_2 at room temperature. Then temperature was slowly elevated (0.5 – 2.0 K/min) up to 363 K. Crystal was left in this temperature for next 30 min. Dehydrated phase $\mathbf{1}^{deh}$ is stable only in the inert atmosphere. Phase $\mathbf{1}^{deh}$ in Apiezon N grease in the air (RT) rehydrates after 2 – 6 h to give $\mathbf{1}^{reh}$, identical to starting crystals of **1**. The FT-IR spectra shows that crystals of $\mathbf{1}^{deh}$ without protection grease rehydrate almost instantaneously when exposed to air. In order to provide evidence as well as good quality of data considering SC-SC transition the procedure was as follows. Firstly, the crystal of **1** was placed into diffractometer in RT and cooled to 100 K (5 K/min) for the measurement. In the second step the crystal was heated again to room temperature (5 K/min). The dehydration process was performed by heating crystal to 363 K (2 K/min), and then the crystal was conditioned in this temperature for next 30 min. After dehydration the crystal was cooled to 100 K (5 K/min), in which the diffraction data for $\mathbf{1}^{deh}$ were collected. In the third step the sample $\mathbf{1}^{deh}$ was heated to RT and left for 6 h in air (process could be accelerated by exposition of crystals on H_2O vapours). As a result, the rehydrated sample was obtained. Finally, the crystal was cooled to 100 K and structural data for $\mathbf{1}^{reh}$ were collected. The high temperature data were collected independently of SC-SC experiment described above. The diffraction data for $\mathbf{1}^{HT}$ were collected directly after inserting crystals in RT. The measurement for $\mathbf{1}^{des,HT}$ was performed by inserting crystal of **1** in RT followed by dehydration process in high temperature and re-cooling to RT (5 K/min).

5.2.3. Synthesis of **2**

1 mL of a freshly prepared H_2O/MeOH (0.05 mL H_2O, 0.95 mL MeOH) solution of TPMA ligand (38.75 mg, 0.13 mmol) was added dropwise to 3 mL of H_2O/MeOH solution (0.15 mL H_2O, 2.85 mL MeOH) of $FeCl_2{\cdot}4H_2O$ (19 mg, 0.096 mmol) and L(+)-ascorbic acid (1.0 mg, 0.006 mmol). The resulting mixture was stirred for 5 min, then 1.5 mL of H_2O/MeOH solution (0.075 mL H_2O, 1.425 mL MeOH) of $TBA_3[W^V(CN)_8]$ (111.9 mg, 0.1 mmol) was added dropwise, while stirring continuously. The solution was stirred for next 20 min, and then the vial was tightly closed and left for crystallization in room temperature. After 3–5 days yellow–brown crystals appeared. The crystals of **2** were identified as $(TBA)_2\{[Fe^{II}(TPMA)]_2[W^V(CN)_8]_2\}{\cdot}6MeOH{\cdot}4H_2O$, based on SC-XRD measurements. The crystals are stable in the mother solution as well as in NVH oil or Apiezon N grease, however, under exposure to air they gradually exchange MeOH molecules to H_2O molecules, which result in air stable composition of $(TBA)_2\{[Fe^{II}(TPMA)]_2[W^V(CN)_8]_2\}{\cdot}2MeOH{\cdot}13H_2O$ ($\mathbf{2}_{solvated}$). Elemental CHN analysis: Calcd. for $\mathbf{2}_{solvated}$: C 45.7 %, H 6.3 % N 16.1 %. Found: C 45.8 %, H 6.3 %, N 16.2 %. Phase purity was confirmed by powder XRD data measured on the crystallites under mother solution (Fig. S10). Due to instability of crystals in air as well as in N_2 purge at high temperatures, the $\mathbf{2}^{HT}$ RT XRD measurement was performed in capillary with drop of mother solution.

5.2.4. Synthesis of **3**

1.25 mL of a freshly prepared H_2O/MeOH solution (0.75 mL H_2O, 0.50 mL MeOH) of TPMA ligand (38.75 mg, 0.13 mmol) was added dropwise to 3.25 mL of H_2O/MeOH solution (1.75 mL H_2O, 1.50 mL MeOH) of $FeCl_2{\cdot}4H_2O$ (19 mg, 0.096 mmol) and L(+)-ascorbic acid (1.0 mg, 0.006 mmol). The resulting solution was stirred for 5 min, then 7.5 mL of H_2O/MeOH solution (4.5 mL H_2O, 3 mL MeOH) of 1,3,5-trihydroxybenzene, H_3PG, (96 mg, 0.76 mmol) was added slowly. Finally, 2.5 mL of H_2O/MeOH solution (1.0 mL H_2O, 1.5 mL MeOH) solution of $TBA_3[W^V(CN)_8]$ (111.9 mg, 0.1 mmol) was added dropwise. The resulting mixture was stirred for next 20 min, and then the vial was tightly closed and left for crystallization in room temperature. After 3–5 days very small yellow–brown crystals appeared. The crystals of **3** were identified as $(TBA)_2\{[Fe^{II}(TPMA)]_2[W^V(CN)_8]_2\}{\cdot}H_3PG{\cdot}4H_2O2MeOH$ (H_3PG = 1,3,5-trihydroxybenzene), based on SC-XRD measurements. The crystals are stable in the mother solution as well as in NVH oil or Apiezon N grease, however, upon exposure to air they gradually exchange the MeOH molecules to H_2O molecules, which result in air stable composition of $(TBA)_2\{[Fe^{II}(TPMA)]_2[W^V(CN)_8]_2\}{\cdot}H_3PG{\cdot}7H_2O$ ($\mathbf{3}_{solvated}$). Elemental CHN analysis: Calcd. for $\mathbf{3}_{solvated}$: C 48.9 %, H 5.7 % N 16.5 %. Found: C 48.8 %, H 5.7 %, N 16.6 %. Phase purity was confirmed by powder XRD data measured on the crystallites under mother solution (Fig. S10).

5.3. Crystal structure solution and refinement

Single crystal X-ray diffraction data for all compounds were collected using a Bruker D8 Quest Eco diffractometer equipped with Photon II detector, Mo Kα (λ = 0.71073 Å) radiation source with a graphite monochromator and the Oxford Cryostream cooling system. For measurement at 100 K the crystals of **1**, **2**, and **3** were taken out of mother solution and covered by NVH immersion oil. Dehydration and rehydration processes of crystal **1** leading to $\mathbf{1}^{des}$ and $\mathbf{1}^{reh}$, respectively, as well as measurements for these phases were performed in Apiezon N grease. Room temperature measurements were performed in NVH immersion oil ($\mathbf{1}^{HT}$), Apiezon N grease ($\mathbf{1}^{des,HT}$) or in capillary with drop of mother solution ($\mathbf{2}^{HT}$), respectively. Data reduction and cell parameter refinement were performed using Apex software with included SAINT and SADABS programs. Intensities of reflections for the sample absorption were corrected using multiscan method. Structures were solved by intrinsic phasing method and refined anisotropically with weighted full-matrix least squares on F^2 using SHELXT [87] and SHELXL [88] programs with Olex 2 graphic interface [89]. In the crystal structures of **2**, $\mathbf{2}^{HT}$, and **3** MeOH and H_2O crystallization molecules disorder is observed, thus we performed solvent disorder modelling. In case of MeOH and H_2O molecules some of atoms were in two or three alternative positions with partial occupancy, which requires an individual cases ISOR or SIMU restraints as well as DFIX restraints on bond lengths (MeOH). In case of **2** and $\mathbf{2}^{HT}$ the solvent molecules were refined isotropically due to significant disorder. Hydrogen atoms within structures

were placed in idealized positions and refined using riding coordinate model with isotropic displacement parameter set at 1.2 – 1.5 times U_{eq} of appropriate carrier atoms. In case of $\mathbf{2}^{HT}$, due to intensive disorder as well as enlarged thermal ellipsoids (due to room temperature measurement) the proper embedment the hydrogen atoms in crystallization molecules was difficult, thus in order to ensure the correct density of crystal and formula of compound, these atoms were only included in the summary formula in structural file. Crystal data and structure refinement parameters are summarized in Table S1-S3. The structural figures in article were prepared using latest version of Mercury software [90]. Continuous shape measure analysis of coordination spheres was performed using SHAPE 2.1 [91]. The crystal structures are deposited in CCDC data base. The deposition numbers are 2,163,156 (**1**) 2,163,157 ($\mathbf{1}^{deh}$), 2,163,158 ($\mathbf{1}^{reh}$), 2,163,159 ($\mathbf{1}^{HT}$), 2,163,160 ($\mathbf{1}^{deh,HT}$), 2,163,161 (**2**), 2,163,162 ($\mathbf{2}^{HT}$), and 2,163,163 (**3**), respectively.

5.4. Methods and techniques

CHN elemental analyses were performed on Micro Cube CHNS analyser. Powder X-ray patterns were collected using Bruker D8 Advance Eco powder diffractometer with spinning capillary and Cu Kα (λ = 1.5418 Å) radiation source. Magnetic measurements were probed with Quantum Design MPMS 3 SQUID magnetometer. Microcrystalline samples were measured in foil bag (**1**) or in sealed glass tube with mother solution under vacuum (**2**). The dc magnetic susceptibilities were measured in the 1.8 – 300 K temperature range with an applied field of 2000 Oe. Isothermal magnetizations were collected at 1.8 K in the 0 – 70 kOe applied dc field range. The magnetic data were corrected for diamagnetic contribution of the foil bag (**1**) or glass tube (**2**) as well as on sample by empirical and Pascal's constants, respectively [92]. The infrared spectra were collected using a Nicolet iN10 MX FT-IR microscope in the transmission mode. Measurements were performed on thin layer of compounds achieved by crushing and stripping of small crystallites. In case of compound **1** in order to record dehydration and rehydration process, the additional measurement in variable temperature cell with purge of N_2 or N_2/H_2O vapour were performed.

CRediT authorship contribution statement

Jedrzej Kobylarczyk: Conceptualization, Syntheses and investigation – co-management, planning and performance, Writing – major contribution the manuscript preparation, review & editing. **Paweł Pakulski:** Syntheses and investigation – planning and performance; Writing – contribution the manuscript preparation, review & editing. **Izabela Potępa:** Syntheses and investigation, Writing – review and editing; **Robert Podgajny:** Funding acquisition, Project management and administration, Conceptualization, Syntheses and investigation – co-management and planning, Writing – major contribution the manuscript preparation, review & editing.

Declaration of Competing Interest

The authors declare that they have no known competing financial interests or personal relationships that could have appeared to influence the work reported in this paper.

Data availability

Data will be made available on request.

Acknowledgements

We gratefully acknowledge the financial support from the National Science Centre (Poland) research project no. UMO-2019/35/B/ST5/01481 (PI R. Podgajny). Measurements were carried out with equipment funded by the European Regional Development Fund in the framework of the Polish Innovation Economy Operational Program (contract no. POIG.02.01.00-12-023/08). Magnetic measurements were performed using equipment funded by Polish Ministry of Science and Higher Education in the framework of Large Research Infrastructure Fund (decision no. 6350/IA/158/2013.1).

Appendix A. Supplementary data

Supplementary data to this article can be found online at https://doi.org/10.1016/j.poly.2022.116028.

References

[1] M. Andruh, Heterotrimetallic complexes in molecular magnetism, Chem. Commun. 54 (2018) 3559–3577, https://doi.org/10.1039/C8CC00939B.
[2] L. Shi, X.-Q. Wei, X. Wang, D. Wu, Research progress in molecular magnetic materials based on the $[Mo(CN)_7]4-$ unit, Sci. Sin. Chim. 50 (2020) 1637–1653, https://doi.org/10.1360/SSC-2020-0122.
[3] S. Chorazy, J.J. Zakrzewski, M. Magott, T. Korzeniak, B. Nowicka, D. Pinkowicz, R. Podgajny, B. Sieklucka, Octacyanidometallates for multifunctional molecule-based materials, Chem. Soc. Rev. 49 (2020) 5945–6001, https://doi.org/10.1039/D0CS00067A.
[4] J. Kobylarczyk, E. Kuzniak, M. Liberka, S. Chorazy, B. Sieklucka, R. Podgajny, Modular approach towards functional multimetallic coordination clusters, Coord. Chem. Rev. 419 (2020), 213394, https://doi.org/10.1016/j.ccr.2020.213394.
[5] J.J. Zakrzewski, M. Liberka, M. Zychowicz, S. Chorazy, Diverse physical functionalities of rare-earth hexacyanidometallate frameworks and their molecular analogues, Inorg. Chem. Front. 8 (2021) 452–483, https://doi.org/10.1039/D0QI01197E.
[6] C. Wang, D. Chang, Q. Gao, C. Liu, Q. Wang, X. Huang, Y. Jia, Large and tunable negative thermal expansion induced by a synergistic effect in $M^{II}_2[M^{IV}(CN)_8]$ Prussian blue analogues, Phys. Chem., Chem. Phys. 22 (2020) 18655–18662, https://doi.org/10.1039/D0CP02191A.
[7] T. Yoshida, K. Nakabayashi, H. Tokoro, M. Yoshikiyo, A. Namai, K. Imoto, K. Chibac, S. Ohkoshi, Extremely low-frequency phonon material and its temperature- and photo-induced switching effects, Chem. Sci. 11 (2020) 8989–8998, https://doi.org/10.1039/D0SC02605K.
[8] W. Sas, D. Pinkowicz, M. Perzanowski, M. Fitta, Magnetic, structural and spectroscopic properties of iron(II)-octacyanoniobate(IV) crystalline film obtained by ion-exchange synthesis, Materials 13 (2020) 3029, https://doi.org/10.3390/ma13133029.
[9] H. Yoshino, N. Tomokage, A. Mishima, B. Le Ouay, R. Ohtani, W. Kosaka, H. Miyasaka, M. Ohba, Guest-selective and reversible magnetic phase switching in a pseudo-pillared-layer porous magnet, Chem. Commun. 57 (2021) 5211–5214, https://doi.org/10.1039/D1CC01526E.
[10] M. Magott, B. Gaweł, M. Sarewicz, M. Reczyński, K. Ogorzały, W. Makowski, D. Pinkowicz, Large breathing effect induced by water sorption in a remarkably stable nonporous cyanide-bridged coordination polymer, Chem. Sci. 12 (2021) 9176–9188, https://doi.org/10.1039/D1SC02060A.
[11] M. Komine, K. Imoto, A. Namai, M. Yoshikiyo, S. Ohkoshi, Photoswitchable nonlinear-optical crystal based on a dysprosium-iron nitrosyl metal assembly, Inorg. Chem. 60 (2021) 2097–2104, https://doi.org/10.1021/acs.inorgchem.0c03493.
[12] R. Jankowski, J.J. Zakrzewski, M. Zychowicz, J. Wang, Y. Oki, S. Ohkoshi, S. Chorazy, B. Sieklucka, SHG-active NIR-emissive molecular nanomagnets generated in layered neodymium(II)–octacyanidometallate(IV) frameworks, J. Mater. Chem. C 9 (2021) 10705–10717, https://doi.org/10.1039/D1TC00825K.
[13] A. Choudhury, C. Pichon, J.-P. Sutter, D. Pamu, B. Sarma, P.P. Mudoi, N. Gogoi, Accessing water processable cyanido bridged chiral heterobimetallic Co(II)–Fe(III) one dimensional network, Chem. Commun. 57 (2021) 207–210, https://doi.org/10.1039/D0CC05356B.
[14] M. Liberka, J.J. Zakrzewski, M. Heczko, M. Reczyński, S. Ohkoshi, S. Chorazy, Solvent- and temperature-driven photoluminescence modulation in porous hofmann-Type Sr^{II}–Re^{V} metal-organic frameworks, Inorg. Chem. 60 (2021) 4093–4107, https://doi.org/10.1021/acs.inorgchem.1c00165.
[15] M. Reczyński, D. Pinkowicz, K. Nakabayashi, C. Näther, J.J. Stanek, M. Kozieł, J. Kalinowska-Tłuścik, B. Sieklucka, S. Ohkoshi, B. Nowicka, Room-temperature bistability in a Ni–Fe chain: electron transfer controlled by temperature, pressure, light, and humidity, Angew. Chem. Int. Ed. 60 (2021) 2330–2338, https://doi.org/10.1002/anie.202012876.
[16] W. Wen, Y.-S. Meng, C.-Q. Jiao, Q. Liu, H.-L. Zhu, Y.-M. Li, H. Oshio, T. Liu, A mixed-valence Fe13 cluster exhibiting metal-to-metal charge-transfer-switched spin crossover, Angew. Chem. Int. Ed. 59 (38) (2020) 16393–16397.
[17] A. Sulaiman, Y.-Z. Jiang, M.K. Javed, S.-Q. Wu, Z.-Y. Li, X.-H. Bu, Tuning of spin-crossover behavior in two cyano-bridged mixed-valence $Fe^{III}_2Fe^{II}$ trinuclear complexes based on a Tp^{R} ligand, Inorg. Chem. Front. 9 (2022) 241–248, https://doi.org/10.1039/D1QI01086G.
[18] D.J. Tranchemontagne, J.L. Mendoza-Cortés, M. O'Keeffe, O.M. Yaghi, Secondary building units, nets and bonding in the chemistry of metal–organic frameworks, Chem. Soc. Rev. 38 (2009) 1257–1283, https://doi.org/10.1039/B817735J.
[19] J.J. Sokol, M.P. Shores, J.R. Long, Giant metal–cyanide coordination clusters: tetracapped edge-bridged cubic $Cr_{12}Ni_{12}(CN)_{48}$ and double face-centered cubic

$Cr_{14}Ni_{13}(CN)_{48}$ species, Inorg. Chem. 41 (2002) 3052–3054, https://doi.org/10.1021/ic0255499.
[20] R. Podgajny, S. Chorąży, W. Nitek, M. Rams, M. Bałanda, B. Sieklucka, $\{Mn^{II}_9W^{V}_6\}_n$ nanowires organized into three-dimensional hybrid network of I^1O^2 topology, Cryst. Growth Des. 10 (2010) 4693–4696, https://doi.org/10.1021/cg100920c.
[21] S. Chorazy, R. Podgajny, W. Nitek, M. Rams, S. Ohkoshi, B. Sieklucka, Supramolecular chains and coordination nanowires constructed of high-spin $Co^{II}_9W^{V}_6$ clusters and 4,4′-bpdo linkers, Cryst. Growth Des. 13 (2013) 3036–3045, https://doi.org/10.1021/cg400448x.
[22] K.E. Funck, M.G. Hilfiger, C.P. Berlinguette, M. Shatruk, W. Wernsdorfer, K. R. Dunbar, Trigonal-bipyramidal metal cyanide complexes: a versatile platform for the systematic assessment of the magnetic properties of prussian blue materials, Inorg. Chem. 48 (2009) 3438–3452, https://doi.org/10.1021/ic801990g.
[23] M. Magott, M. Sarewicz, S. Buda, D. Pinkowicz, Heterotrimetallic cyanide-bridged 3d–4d-5d frameworks based on a photomagnetic secondary building unit, Inorg. Chem. 59 (2020) 8925–8934, https://doi.org/10.1021/acs.inorgchem.0c00737.
[24] G.N. Newton, M. Nihei, H. Oshio, Cyanide-bridged molecular squares – the building units of prussian blue, Eur. J. Inorg. Chem. 20 (2011) 3031–3042, https://doi.org/10.1002/ejic.201100407.
[25] D. Aguilà, Y. Prado, E.S. Koumousi, C. Mathonière, R. Clérac, Switchable Fe/Co Prussian blue networks and molecular analogues, Chem. Soc. Rev. 45 (2016) 203–224, https://doi.org/10.1039/C5CS00321K.
[26] M. Nihei, Molecular prussian blue analogues: from bulk to molecules and low-dimensional aggregates, Chem. Lett. 49 (2020) 1206–1215, https://doi.org/10.1246/cl.200428.
[27] P.P. Mudoi, B. Sarma, A. Choudhury, N. Gogoi, Evidence of protonation induced intra-molecular metal-to-metal charge transfer in a highly symmetric cyanido bridged Fe2Ni2 molecular square, Dalton Trans. 50 (2021) 2057–2066, https://doi.org/10.1039/D0DT02826F.
[28] M. Nihei, Y. Yanai, I.-J. Hsu, Y. Sekine, H. Oshio, A hydrogen-bonded cyanide-bridged $[Co_2Fe_2]$ Square complex exhibiting a three-step spin transition, Angew. Chem. Int. Ed. 56 (2017) 591–594, https://doi.org/10.1002/anie.201610268.
[29] Y. Sekine, M. Nihei, H. Oshio, Dimensionally controlled assembly of an external stimuli-responsive $[Co_2Fe_2]$ complex into supramolecular hydrogen-bonded networks, Chem. Eur. J. 23 (2017) 5193–5197, https://doi.org/10.1002/chem.201605817.
[30] M. Nihei, Y. Yanai, D. Natke, R. Takayama, M. Kato, Y. Sekine, F. Renz, H. Oshio, Solid-state hydrogen-bond alterations in a $[Co_2Fe_2]$ complex with bifunctional hydrogen-bonding donors, Chem. Eur. J. 25 (2019) 7449–7452, https://doi.org/10.1002/chem.201901383.
[31] S. Kamilya, S. Ghosh, Y. Li, P. Dechambenoit, M. Rouzières, R. Lescouëzec, S. Mehta, A. Mondal, Two-step thermoinduced metal-to-metal electron transfer and ON/OFF photoswitching in a molecular $[Fe_2Co_2]$ square complex, Inorg. Chem. 59 (2020) 11879–11888, https://doi.org/10.1021/acs.inorgchem.0c02053.
[32] L. Meng, Y.-F. Deng, Y.-Z. Zhang, Anion-dependent electron transfer in the cyanide-bridged $[Fe_2Co_2]$ capsules, Inorg. Chem. 50 (2021) 14330–14335, https://doi.org/10.1021/acs.inorgchem.1c01952.
[33] A. Mondal, Y. Li, L.-M. Chamoreau, M. Seuleiman, L. Rechignat, A. Bousseksou, M.-L. Boillot, R. Lescouëzec, Photo- and thermo-induced spin crossover in a cyanide-bridged MoV2FeII2 rhombus molecule, Chem. Commun. 50 (2014) 2893–2895, https://doi.org/10.1039/C3CC49164A.
[34] K. Kaushik, S. Ghosh, S. Kamilya, M. Rouzières, S. Mehta, A. Mondal, Reversible photo- and thermo-induced spin-state switching in a heterometallic 5d–3d W2Fe2 molecular square complex, Inorg. Chem. 60 (2021) 7545–7552, https://doi.org/10.1021/acs.inorgchem.1c01014.
[35] S. Chorazy, R. Podgajny, K. Nakabayashi, J. Stanek, M. Rams, B. Sieklucka, S. Ohkoshi, FeII spin-crossover phenomenon in the pentadecanuclear Fe9[Re(CN)8]6 spherical cluster, Angew. Chem. Int. Ed. 54 (2015) 5093–5097, https://doi.org/10.1002/anie.201500288.
[36] S. Chorazy, J.J. Stanek, W. Nogaś, A.M. Majcher, M. Rams, M. Kozieł, E. Juszyńska-Gałązka, K. Nakabayashi, S. Ohkoshi, B. Sieklucka, R. Podgajny, Tuning of charge transfer assisted phase transition and slow magnetic relaxation functionalities in Fe9–xCox[W(CN)8]6 (x = 0–9) molecular solid solution, J. Am. Chem. Soc. 138 (2016) 1635–1646, https://doi.org/10.1021/jacs.5b11924.
[37] S. Chorazy, J.J. Stanek, J. Kobylarczyk, S. Ohkoshi, B. Sieklucka, R. Podgajny, Modulation of the FeII spin crossover effect in the pentadecanuclear Fe9[M(CN)8]6 (M = Re, W) clusters by facial coordination of tridentate polyamine ligands, Dalton Trans. 46 (2017) 8027–8036, https://doi.org/10.1039/C7DT01416C.
[38] J. Kobylarczyk, M. Liberka, J.J. Stanek, B. Sieklucka, R. Podgajny, Tuning of the phase transition between site selective SCO and intermetallic ET in trimetallic magnetic cyanido-bridged clusters, Dalton Trans. 49 (2020) 17321–17330, https://doi.org/10.1039/D0DT03340E.
[39] M. Arczyński, J. Stanek, B. Sieklucka, K.R. Dunbar, D. Pinkowicz, Site-selective photoswitching of two distinct magnetic chromophores in a propeller-like molecule to achieve four different magnetic states, J. Am. Chem. Soc. 141 (2019) 19067–19077, https://doi.org/10.1021/jacs.9b09576.
[40] R. Jankowski, M. Reczyński, S. Chorazy, M. Zychowicz, M. Arczyński, M. Kozieł, K. Ogorzały, W. Makowski, D. Pinkowicz, B. Sieklucka, Guest-dependent pressure-induced spin crossover in $Fe^{II}_4[M^{IV}(CN)_8]_2$ (M=Mo, W) cluster-based material showing persistent solvent-driven structural transformations, Chem. Eur. J. 26 (2020) 11187–11198, https://doi.org/10.1002/chem.202000146.
[41] L. Zhao, Y.-S. Meng, Q. Liu, O. Sato, Q. Shi, H. Oshio, T. Liu, Switching the magnetic hysteresis of an $[Fe^{II}$–NC–$W^{V}]$-based coordination polymer by photoinduced reversible spin crossover, Nat. Chem. 13 (2021) 698–704, https://doi.org/10.1038/s41557-021-00695-1.
[42] A. Diebold, K.S. Hagen, Iron(II) polyamine chemistry: variation of spin State and coordination number in solid state and solution with iron(II) Tris(2-pyridylmethyl) amine complexes, Inorg. Chem. 37 (1998) 215–223, https://doi.org/10.1021/ic971105e.
[43] Y. Zang, J. Kim, Y. Dong, E.C. Wilkinson, E.H. Appelman, L. Que, Models for nonheme iron intermediates: structural basis for tuning the spin states of Fe(TPA) complexes, J. Am. Chem. Soc. 119 (1997) 4197–4205, https://doi.org/10.1021/ja9638521.
[44] B. Li, R.-J. Wei, J. Tao, R.-B. Huang, L.-S. Zheng, Z. Zheng, Solvent-induced transformation of single crystals of a spin-crossover (SCO) compound to single crystals with two distinct SCO centers, J. Am. Chem. Soc. 132 (2010) 1558–1566, https://doi.org/10.1021/ja909695f.
[45] R.-J. Wei, J. Tao, R.-B. Huang, L.-S. Zheng, Reversible and irreversible vapor-induced guest molecule exchange in spin-crossover compounds, Inorg. Chem. 50 (2011) 8553–8564, https://doi.org/10.1021/ic201142t.
[46] X.-P. Sun, R.-J. Wei, Z.-S. Yao, J. Tao, Solvent effects on the structural packing and spin-crossover properties of a mononuclear iron(II) complex, Cryst. Growth Des. 18 (2018) 6853–6862, https://doi.org/10.1021/acs.cgd.8b01079.
[47] V. García-López, J.C. Waerenborgh, B.J.C. Vieira, M. Clemente-León, E. Coronado, Iron(II) complexes of tris(2-pyridylmethyl)amine (TPMA) and neutral bidentate ligands showing thermal- and photo-induced spin crossover, Dalton Trans. 47 (2018) 9156–9163, https://doi.org/10.1039/C8DT01425F.
[48] H. Phan, S.M. Benjamin, E. Steven, J.S. Brooks, M. Shatruk, Photomagnetic response in highly conductive iron(II) spin-crossover complexes with TCNQ radicals, Angew. Chem. Int. Ed. 54 (2015) 823–827, https://doi.org/10.1002/anie.201408680.
[49] H.V. Phan, P. Chakraborty, M. Chen, Y.M. Calm, K. Kovnir, L.K. Keniley Jr., J. M. Hoyt, E.S. Knowles, C. Besnard, M.W. Meisel, A. Hauser, C. Achim, M. Shatruk, Heteroleptic Fe^{II} complexes of 2,2′-biimidazole and its alkylated derivatives: spin-crossover and photomagnetic behavior, Chem. Eur. J. 18 (2012) 15805–15815, https://doi.org/10.1002/chem.201202045.
[50] A. Schober, S. Demeshko, F. Meyer, Spin state variations and spin-crossover in diiron(II) complexes of bis(pentadentate) pyrazolate-based ligands, Z. Anorg. Allg. Chem. 644 (2018) 719–728, https://doi.org/10.1002/zaac.201800148.
[51] S.R. Batten, J. Bjernemose, P. Jensen, B.A. Leita, K.S. Murray, B. Moubaraki, J. P. Smith, H. Toftlund, Designing dinuclear iron(II) spin crossover complexes. Structure and magnetism of dinitrile-, dicyanamido-, tricyanomethanide-, bipyrimidine- and tetrazine-bridged compounds, Dalton Trans. (2004) 3370–3375, https://doi.org/10.1039/B410425K.
[52] R.-J. Wei, Q. Huo, J. Tao, R.-B. Huang, L.-S. Zheng, Spin-crossover Fe^{II}_4 squares: two-step complete spin transition and reversible single-crystal-to-single-crystal transformation, Angew. Chem., Int. Ed. 50 (2011) 8940–8943, https://doi.org/10.1002/anie.201103648.
[53] R.-J. Wei, J. Tao, R.-B. Huang, L.-S. Zheng, Anion-dependent spin crossover and coordination assembly based on $[Fe(tpa)]^{2+}$ [tpa = tris(2-pyridylmethyl)amine] and $[N(C_N)^2]^-$: square, zigzag, dimeric, and [4+1]-cocrystallized complexes, Eur. J. Inorg. Chem. 2013 (5-6) (2013) 916–926.
[54] E. Milin, S. Belaïd, V. Patinec, S. Triki, G. Chastanet, M. Marchivie, Dinuclear spin-crossover complexes based on tetradentate and bridging cyanocarbanion ligands, Inorg. Chem. 55 (2016) 9038–9046, https://doi.org/10.1021/acs.inorgchem.6b01542.
[55] O. Hietsoi, P.W. Dunk, H.D. Stout, A. Arroyave, K. Kovnir, R.E. Irons, N. Kassenova, R. Erkasov, C. Achim, M. Shatruk, Spin crossover in tetranuclear Fe(II) complexes, $\{[(tpma)Fe(\mu\text{-}CN)]_4\}X_4$ (X = ClO^-_4, BF^-_4), Inorg. Chem. 53 (2014) 13070–13077, https://doi.org/10.1021/ic502215h.
[56] M. Nihei, M. Ui, H. Oshio, Cyanide-bridged tri- and tetra-nuclear spin crossover complexes, Polyhedron 28 (2009) 1718–1721, https://doi.org/10.1016/j.poly.2008.10.051.
[57] M. Nihei, M. Ui, M. Yokota, L. Han, A. Maeda, H. Kishida, H. Okamoto, H. Oshio, Two-step spin conversion in a cyanide-bridged ferrous square, Angew. Chem. Int. Ed. 44 (2005) 6484–6487, https://doi.org/10.1002/anie.200502216.
[58] C. Zheng, J. Xu, F. Wang, J. Tao, D. Li, Spin crossover and reversible single-crystal to single-crystal transformation behaviour in two cyanide-bridged mixed-valence FeIII2FeII2 clusters, Dalton Trans. 45 (2016) 17254–17263, https://doi.org/10.1039/C6DT03436E.
[59] I. Boldog, F.J. Muñoz-Lara, A.B. Gaspar, M.C. Muñoz, M. Seredyuk, J.A. Real, Polynuclear spin crossover complexes: synthesis, structure, and magnetic behavior of $[Fe_4(\mu\text{-}CN)_4(phen)_4(L)_2)]^{4+}$ Squares, Inorg. Chem. 48 (2009) 3710–3719, https://doi.org/10.1021/ic802306r.
[60] A. Dragulescu-Andrasi, O. Hietsoi, Ö. Üngör, P.W. Dunk, V. Stubbs, A. Arroyave, K. Kovnir, M. Shatruk, Dicyanometalates as building blocks for multinuclear iron (II) spin-crossover complexes, Inorg. Chem. 58 (2019) 11920–11926, https://doi.org/10.1021/acs.inorgchem.9b01121.
[61] D. Pinkowicz, R. Podgajny, B. Sieklucka, Molecular magnetic sponges, in: B. Sieklucka, D. Pinkowicz (Eds.), Molecular Magnetic Materials: Concepts and Applications, Wiley-VCH Verlag GmbH & Co. KGaA, Weinheim, Germany, 2017, pp. 279–300.
[62] K. Chen, L. Que, Stereospecific alkane hydroxylation by non-heme iron catalysts: mechanistic evidence for an Fe^{V}=O active species, Am. Chem. Soc. 123 (2001) 6327–6337, https://doi.org/10.1021/ja010310x.
[63] S. McArthur, M.C. Baird, Oxyfunctionalization of polystyrene by hydrogen peroxide using non-heme iron catalysts, Eur. Polym. J. 55 (2014) 170–178, https://doi.org/10.1016/j.eurpolymj.2014.03.028.
[64] R. Santra, K. Biradha, Solid state double [2 + 2] photochemical reactions in the co-crystal forms of 1,5-bis(4-pyridyl)-1,4-pentadiene-3-one: establishing mechanism

using single crystal X-ray, UV and 1H NMR, CrystEngComm 13 (2011) 3246–3257, https://doi.org/10.1039/C0CE00612B.
[65] R. Dubey, G.R. Desiraju, Combinatorial crystal synthesis: structural landscape of phloroglucinol:1,2-bis(4-pyridyl)ethylene and phloroglucinol:phenazine, Angew. Chem. Int. Ed. 53 (2014) 13178–13182, https://doi.org/10.1002/anie.201402668.
[66] L.H. Thomas, G.A. Craig, C.A. Morrison, A.M. Reilly, C.C. Wilson, New route to local order models for disordered crystalline materials: diffuse scattering and computational modeling of phloroglucinol dihydrate, Cryst. Growth Des. 11 (2011) 2045–2049, https://doi.org/10.1021/cg101704h.
[67] C. Guo, Q. Zhang, B. Zhu, Z. Zhang, X. Ma, W. Dai, X. Gong, G. Ren, X. Mei, Drug-drug cocrystals provide significant improvements of drug properties in treatment with progesterone, Cryst. Growth Des. 20 (2020) 3053–3063, https://doi.org/10.1021/acs.cgd.9b01688.
[68] M.P. Singh, J.B. Baruah, Detection of hydroxyaromatics in a superior manner by a water soluble fluorescent iron-complex, Inorg. Chim. Acta 504 504 (2020) 119467.
[69] B. Sarma, L. Sreenivas Reddy, A. Nangia, The role of π-stacking in the composition of phloroglucinol and phenazine cocrystals, Cryst Growth Des. 8 (2008) 4546–4552, https://doi.org/10.1021/cg800585d.
[70] D.E. Braun, D.A. Tocher, S.L. Price, U.J. Griesser, The complexity of hydration of phloroglucinol: A comprehensive structural and thermodynamic characterization, J. Phys. Chem. B 116 (2012) 3961–3972, https://doi.org/10.1021/jp211948q.
[71] S. Shanmugaraju, A.K. Bar, P.S. Mukherjee, Ruthenium–oxygen coordination-driven self-assembly of a Ru_8^{II} incomplete prism: synthesis, structure, and shape-selective molecular recognition study, Inorg. Chem. 49 (2010) 10235–10237, https://doi.org/10.1021/ic101823s.
[72] D. Shin, In Su Lee, Y. Chung, Crystal engineering with structurally flexible 1,1′-substituted ferrocenes for nonlinear optical materials, Eur. J. Inorg. Chem. 2003 (12) (2003) 2311–2317.
[73] K.K. Arora, M.S. Talwelkar, V.R. Pedireddi, Supramolecular synthesis of some molecular adducts of 4,4′-bipyridine N, N′-dioxide, New J. Chem. 33 (2009) 57–63, https://doi.org/10.1039/B807853J.
[74] K. Shankar, M.P. Singh, J.B. Baruah, Extent of protonation of 4,4′-bipyridinium cations and nature of host influences the amount of guest intake by cobalt(II) 2,6-pyridinedicarboxylate, Inorg. Chim. Acta 469 (2018) 440–446, https://doi.org/10.1016/j.ica.2017.09.055.
[75] M. Pfletscher, C. Wölper, J.S. Gutmann, M. Mezger, M. Giese, A modular approach towards functional supramolecular aggregates – subtle structural differences inducing liquid crystallinity, Chem. Commun. 52 (2016) 8549–8552, https://doi.org/10.1039/C6CC03966A.
[76] M. Giese, T. Krappitz, R.Y. Dong, C.A. Michal, W.Y. Hamad, B.O. Patrick, M. J. MacLachlan, Tuning the photonic properties of chiral nematic mesoporous organosilica with hydrogen-bonded liquid-crystalline assemblies, J. Mater. Chem. C 3 (2015) 1537–1545, https://doi.org/10.1039/C4TC02602K.
[77] M. Pfletscher, S. Hölscher, C. Wölper, M. Mezger, M. Giese, Structure-property relationships in hydrogen-bonded liquid crystals, Chem. Mater. 29 (2017) 8462–8471, https://doi.org/10.1021/acs.chemmater.7b03182.
[78] B. Sieklucka, New donor–acceptor system based on $[Pt(NH_3)_4]^{2+}$ and $[W(CN)_8]^{3-}$ ions, J. Chem. Soc., Dalton Trans. (1997) 869–872, https://doi.org/10.1039/A605218E.
[79] M.F.A. Hendrickx, L.F. Chibotaru, A. Ceulemans, The electronic structure and spectrum of $Mo(CN)_8^{3-}$, Inorg. Chem. 42 (2003) 590–597, https://doi.org/10.1021/ic0258734.
[80] S. Kawabata, K. Nakabayashi, K. Imoto, S.-I. Ohkoshi, Spin crossover phenomenon in a three-dimensional cyanido-bridged Fe^{II}–Mo^{IV} assembly, J. Appl. Phys. 129 (10) (2021) 105501.
[81] W. Kosaka, H. Tokoro, T. Matsuda, K. Hashimoto, S. Ohkoshi, Extremely gradual spin-crossover phenomenon in a cyano-bridged Fe−Mo bimetallic assembly, J. Phys. Chem. C 113 (2009) 15751–15755, https://doi.org/10.1021/jp902735v.
[82] S. Chorazy, R. Podgajny, W. Nogaś, W. Nitek, M. Kozieł, M. Rams, E. Juszyńska-Gałązka, J. Żukrowski, C. Kapusta, K. Nakabayashi, T. Fujimoto, S. Ohkoshi, B. Sieklucka, Charge transfer phase transition with reversed thermal hysteresis loop in the mixed-valence $Fe_9[W(CN)_8]_6{\cdot}x$MeOH cluster, Chem. Commun. 50 (2014) 3484–3487, https://doi.org/10.1039/C3CC48029A.
[83] R. Podgajny, T. Korzeniak, K. Stadnicka, Y. Dromzée, N.W. Alcock, W. Errington, K. Kruczała, M. Bałanda, T.J. Kemp, M. Verdaguer, B. Sieklucka, Coordination polymers based on octacyanometalates(IV, V) (M = Mo, W) and aliphatic polyamine copper(II) tectons with $[_N3]$ donor atom sets, Dalton Trans. (2003) 3458–3468, https://doi.org/10.1039/B306422K.
[84] M. Arczyński, M. Rams, J. Stanek, M. Fitta, B. Sieklucka, K.R. Dunbar, D. Pinkowicz, A family of octahedral magnetic molecules based on $[Nb^{IV}(CN)_8]^{4-}$, Inorg. Chem. 56 (2017) 4021–4027, https://doi.org/10.1021/acs.inorgchem.6b03134.
[85] D. Matoga, J. Szklarzewicz, M. Mikuriya, $[PPh_4]_3[W(CN)_7(O_2)]{\cdot}4H_2O$ as the representative of the $[M(L)_7(LL)]$ class for nine-coordinate complexes, Inorg. Chem. 45 (2006) 7100–7104, https://doi.org/10.1021/ic060523t.
[86] Z. Tyeklar, R.R. Jacobson, N. Wei, N.N. Murthy, J. Zubieta, K.D. Karlin, Reversible reaction of dioxygen (and carbon monoxide) with a copper(I) complex. X-ray structures of relevant mononuclear Cu(I) precursor adducts and the trans-(.mu.-1,2-peroxo)dicopper(II) product, J. Am. Chem. Soc. 115 (1993) 2677–2689, https://doi.org/10.1021/ja00060a017.
[87] G. Sheldrick, A short history of SHELX, Acta Crystallogr. Sect. A: Found. Crystallogr. 64 (2008) 112–122, https://doi.org/10.1107/S0108767307043930.
[88] G. Sheldrick, Crystal structure refinement with SHELXL, Acta Crystallogr, Sect. C: Struct. Chem. 71 (2015) 3–8, https://doi.org/10.1107/S2053229614024218.
[89] O.V. Dolomanov, L.J. Bourhis, R.J. Gildea, J.A.K. Howard, H. Puschmann, OLEX2: a complete structure solution, refinement and analysis program, J. Appl. Crystallogr. 42 (2009) 339–341, https://doi.org/10.1107/S0021889808042726.
[90] C.F. Macrae, I. Sovago, S.J. Cottrell, P.T.A. Galek, P. McCabe, E. Pidcock, M. Platings, G.P. Shields, J.S. Stevens, M. Towler, P.A. Wood, Mercury 4.0: from visualization to analysis, design and prediction, J. Appl. Cryst. 53 (2020) 226–235, https://doi.org/10.1107/S1600576719014092.
[91] D. Casanova, J. Cirera, M. Llunell, P. Alemany, D. Avnir, S. Alvarez, Minimal distortion pathways in polyhedral rearrangements, J. Am. Chem. Soc. 126 (2004) 1755–1763, https://doi.org/10.1021/ja036479n.
[92] G.A. Bain, J.F. Berry, Diamagnetic corrections and Pascal's constants, J. Chem. Educ. 85 (2008) 532–536, https://doi.org/10.1021/ed085p532.